Journal of Petroleum Science and Engineering 213 (2022) 110469

Contents lists available at ScienceDirect

Journal of Petroleum Science and Engineering

journal homepage: www.elsevier.com/locate/petrol

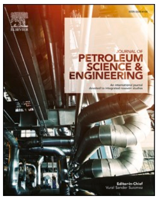

A single-phase diffusion model for gas injection in tight oil reservoirs

Sofiane Haythem Achour, Ryosuke Okuno *

Hildebrand Department of Petroleum & Geosystems Engineering, The University of Texas at Austin, 200 E. Dean Keeton Street, Stop C0300, Austin, TX, 78712, USA

ARTICLE INFO

Keywords:
Dusty gas model
Diffusion
Tight reservoirs
Gas injection
Non-ideal mixing

ABSTRACT

This paper presents a mechanistic simulation study of one-dimensional multicomponent diffusion when the miscible injectant diffuses into a tight porous medium through the fracture/matrix interface with constant pore volume and temperature. The numerical implementation of diffusion based on the dusty gas model uses the fugacity gradient for each component in the mixture as the driving force to the diffusive flux. The Peng-Robinson equation of state is used to model the non-ideal interactions among components in the miscible diffusive process. Phase stability analysis by minimization of the Helmholtz free energy is performed for each grid block at every time step to ensure that mixtures are single-phase fluids throughout the simulation.

The main novelty of this paper lies in the diffusion model and its theoretical analysis, in which the fluid non-ideality affects the multicomponent diffusion through two pathways: the fugacity coefficients and the volume change on mixing that causes local pressures to change under ultra-low permeability in tight porous media. Previous studies based on the Maxwell-Stefan model did not consider the latter pathway, while others based on Fick's law are even more simplistic by not considering the non-ideal chemical potential.

Analysis in this research showed that the Maxwell-Stefan model was inconsistent with its own assumption of no pressure gradient when non-ideal mixing was considered for tight reservoirs. The dusty gas model does not have this issue because it allows for pressure gradients to drive mass transfer by Knudsen diffusion. The non-ideal interaction of components should be properly characterized and utilized to enhance the early-time flux through the fracture/matrix interface in miscible gas injection into a tight reservoir. Case studies show that the volume change on mixing may substantially increase local pressures and the rate of mass transfer in tight reservoirs. Also, the fugacity coefficients of oil components at infinite dilution in the solvent had a major influence on the rate of diffusion. These two factors highlight the importance of properly characterizing reservoir fluids through an equation of state.

CRediT author statement

Sofiane Haythem Achour: Data curation; Formal analysis; Investigation; Methodology; Validation; Visualization; Writing – original draft. Ryosuke Okuno: Conceptualization; Formal analysis; Funding acquisition; Investigation; Methodology; Project administration; Resources; Supervision; Validation; Writing – review & editing.

1. Introduction

Diffusion has been studied as one of the main factors that affect the efficiency of solvent injection in tight reservoirs, where the permeability can be as low as a few nanodarcies (Jia et al., 2018; Tran et al., 2021). Viscous flow in tight reservoir rocks is considerably slower than in conventional reservoirs, and other mass-transport mechanisms can become relatively important. For example, Wan and Sheng (2015) reported Péclet numbers less than 0.01 for flow in tight reservoirs, indicating that diffusion dominated the fluid flow (Peters, 2012). Similarly, Zhang et al. (2015) discussed that Knudsen numbers greater than 0.01 were possible in shale gas and that Knudsen diffusion represented an important contribution to mass transport.

Several models with/without Darcy flow have been developed to study the effects of different injection strategies including solvent properties, injection pressure, and huff-and-puff cycles. Many simplifying assumptions were used to develop those models. For example, Fick's law was implemented with constant diffusion coefficients by Cronin et al. (2019, 2021). Fick's law only accounts for the diffusion driven by density gradients and ignores the effects of non-ideal mixing on the diffusion. Cronin et al. (2019, 2021) found that density was the dominating factor influencing the rate of diffusion. Yanze and Clemens

---

* Corresponding author.
E-mail address: okuno@utexas.edu (R. Okuno).

https://doi.org/10.1016/j.petrol.2022.110469
Received 6 January 2022; Received in revised form 21 March 2022; Accepted 23 March 2022
Available online 28 March 2022

(2012) implemented Fick's law in conjunction with Darcy's law to study the mixing behavior of solvent and oil in tight reservoirs. They confirmed that diffusion was a very important factor even at a permeability of 5 mD, though the simplified model did not allow them to identify factors that maximize the rate of diffusion. Wan and Sheng (2015) implemented Fick's law with composition-dependent diffusion coefficients and Darcy's law, and compared the recovery with and without diffusion for shale.

Other approaches commonly employed are the generalized Fick's law based on the Maxwell-Stefan diffusion model. Hoteit (2013) implemented the Maxwell-Stefan model in a reservoir simulator and set the permeability to an "infinitely low absolute" value to demonstrate the self-consistency of the Maxwell-Stefan model. The results shown in Hoteit (2013) will be particularly discussed later in this paper. Hoteit and Firoozabadi (2009) and Moortgat and Firoozabadi (2010) combined the Maxwell-Stefan model with Darcy flow in a compositional simulator and found that the addition of diffusion mattered most under the minimum miscibility pressure. Shojaei and Jessen (2014) implemented the Maxwell-Stefan model with Darcy's law and showed that Fick's law was unable to predict diffusion behavior caused by non-ideal mixing effects. Mohebbinia and Wong (2017) implemented the Maxwell Stefan model using the chemical potential gradient as the driving force for diffusion; however, this driving force cannot be computed with a boundary condition of pure solvent composition as will be discussed in this paper. Babaei et al. (2018) implemented the Maxwell-Stefan diffusion with Darcy's law using molecular dynamics simulation to estimate the diffusion coefficients through not only the oil and gas but also the water phase. This approach enabled to study enhanced diffusion of CO_2 through the water phase, which involves highly non-ideal mixtures. The formulation of the Maxwell-Stefan model uses the isothermal isobaric chemical potential gradient as the main driving force for diffusion. However, no justification was given for omitting the effect of pressure on the chemical potential gradient; i.e., the non-ideality of fluids was considered partly in the chemical potential, but the pressure change due to the non-ideal mixing and its impact on chemical potential were ignored. In addition, the Maxwell-Stefan model has been found insufficient to fit experimental data of diffusion in porous media. Hoteit (2013) had to use two different multipliers for the diagonal and off-diagonal terms of the diffusion coefficient matrix in order to fit experimental data. Imai et al. (2012) had to use similar multiplying factors to match experimental data. Bhatia et al. (2011) noted that this modification was often necessary to match experimental data of diffusion.

The dusty gas model is a foundational model for transport through porous media as commonly used in chemical engineering. It contains bulk diffusion, Knudsen diffusion, and viscous displacement. This enables to model transitional flow regimes where multiple transport mechanisms take place simultaneously. For example, the Klinkenberg slip can be derived when including the viscous displacement and Knudsen diffusion terms from the dusty gas model (Kerkhof and Geboers, 2005; Sakhaee-Pour and Bryant, 2012). This is especially useful since liquid phases have been shown to slip on pore-walls (Afsharpoor and Javadpour, 2016). Cihan et al. (2019) used this model to account for the effect of pore wall potential interactions on the rate of diffusion. However, their method used computationally expensive engineering density functional theory and only allows for simulation across short distances.

Burrows et al., P2020 recently published a comprehensive literature review on enhanced oil recovery in tight reservoirs. Their review indicated that it was still not clear what would determine an optimal injection composition for a given tight-oil reservoir. One major factor that could influence the efficiency of various solvents is multicomponent diffusion. To the best of our knowledge, however, it is not common practice to design an injection composition considering the diffusive transport in tight reservoirs.

In this paper, we present a new formulation for simulation of purely diffusive transport in miscible solvent injection in tight reservoirs. The formulation is based on the dusty gas model (Mason and Malinauskas, 1983; Krishna and Wesselingh, 1997). The correlation of Leahy-Dios and Firoozabadi (2007) is used to model the composition-dependent diffusivities along with the LBC correlation (Lohrenz et al., 1964) for the viscosities. The pressure and chemical potential gradients are computed using the Peng-Robinson equation of state (PR EOS) (Robinson and Peng, 1978).

1.1. Diffusion model

This section introduces a new approach to modeling the diffusive fluxes in tight reservoirs using the dusty gas model with the following assumptions:

- No viscous flow because of the extremely low permeability of the porous medium
- No external forces with electrically neutral fluid
- Constant temperature.

The main objective of this research is to study the effects of non-ideal interactions among components on the oil production based on the diffusive transport of miscible solvents in tight oil reservoirs. In particular, the formulation allows for local pressure changes caused by volume change on mixing, which affect the multicomponent diffusion through chemical potentials. Appendix A explains why the two most commonly used diffusion models, Fick's law and the Maxwell-Stefan model, are unable to account for the effects that we would like to model. It also presents the original form of the dusty gas model.

Among many other factors, inclusion of multiple phases, sorbed layers, and convective transport is expected to be important for studying a wider range of operating conditions for gas EOR in tight formations. Also, solution of such coupled phenomena by itself requires an extensive numerical study. Hence, the current paper is focused on theoretical analysis of single-phase diffusion using the dusty gas model with fluid non-ideality, which represents the main novelty of the current paper.

Eq. (A1) can then be simplified to

$$-\frac{x_i}{RT}\nabla_{T,P}\mu_i - \frac{x_i\overline{V}_i}{RT}\nabla P = \underline{V}\sum_{\substack{j=1\\ j\neq i}}^{N_c}\frac{x_j\dot{n}_i - x_i\dot{n}_j}{\text{Đ}^e_{ij}} + \underline{V}\frac{\dot{n}_i}{\text{Đ}^e_{iM}}, \tag{1}$$

where $i = 1, 2, \ldots, N_c$. Summing Eq. (1) for the N_C components gives an expression for the overall Knudsen diffusion driven by the pressure gradient

$$-\frac{\nabla P}{RT} = \sum_{i=1}^{N_c}\frac{\dot{n}_i}{\text{Đ}^e_{iM}}, \tag{2}$$

where $i = 1, 2, \ldots, N_c$. Eq. (2) shows that the overall flow direction is determined by the pressure gradient. This will be used in the next section for the numerical solution scheme. Grouping the first two terms on the left-hand side of Eq. (1) gives

$$-\frac{\nabla_T f_i}{\varphi_i P} = \underline{V}\sum_{\substack{j=1\\ j\neq i}}^{N_c}\frac{x_j\dot{n}_i - x_i\dot{n}_j}{\text{Đ}^e_{ij}} + \underline{V}\frac{\dot{n}_i}{\text{Đ}^e_{iM}}, \tag{3}$$

where $i = 1, 2, \ldots, N_c$, or equivalently,

$$\dot{\boldsymbol{n}} = -\mathcal{D}\nabla_T\mathbf{f}, \tag{4}$$

where $\nabla_T\mathbf{f}$ is the fugacity gradient as the driving force for diffusion. Mohebbinia and Wong (2017) were the first to directly use the chemical potential as the driving force. However, their approach causes problems when the chemical potential of component i in the mixture is undefined where $x_i = 0$, and its limit at infinite dilution ($x_i \rightarrow 0$) is $-\infty$. Eq. (4) uses fugacity, instead of chemical potential, for the driving force term. This approach improves the problem mentioned above as the fugacity of a component i at inifinite dilution in the solvent is defined as zero.

Case 2 will analyze the different factors that can influence this driving force. $\mathcal{D}$ is a Nc × Nc matrix of diffusion coefficients defined as

$$\mathcal{D} = c\mathcal{B}^{-1}(\boldsymbol{\varphi}P)^{-1}, \tag{5}$$

where $(\boldsymbol{\varphi}P)^{-1}$ is the diagonal matrix, of which the diagonal elements contain the inverse of the fugacity coefficients and pressure. The $\mathcal{B}$ matrix is defined as

$$\mathcal{B} : \mathscr{B}_{ij} = \begin{cases} \sum_{\substack{k=1 \\ i \neq k}}^{N_c} \frac{x_k}{Đ_{ik}^e} + \frac{1}{Đ_{iM}^e} : i = j \\ -\frac{x_i}{Đ_{ij}^e} \quad : i \neq j \end{cases}. \tag{6}$$

In general, the elements of $\mathcal{D}$ are positive and dependent on composition and pressure.

2. Solution method

We solve the continuity equation

$$\frac{\varphi \partial c\mathbf{x}}{\partial t} = -\nabla \dot{\boldsymbol{n}}, \tag{7}$$

using Eq. (3) for the diffusive flux. A common simplification used to model flow from a hydraulically fractured horizontal well is one-dimensional flow from the fracture (x = 0) to the fracture spacing half-length L with a no-flow boundary condition (BC) (Patzek et al., 2019; Cronin et al., 2019). The fracture can be modeled as a constant composition and pressure BC. Fig. 1 shows a schematic for the model.

The discretized continuity equation for grid block k at time step t is then

$$\mathbf{n}^{t+1} = \mathbf{n}^t + \Delta t\mathbf{R}^{k-\frac{1}{2}}\left(\mathbf{f}^k - \mathbf{f}^{k-1}\right) - \Delta t\mathbf{R}^{k+\frac{1}{2}}\left(\mathbf{f}^{k+1} - \mathbf{f}^k\right), \tag{8}$$

where **n** and **f** are the vectors containing the number of moles and fugacity for each component, respectively. $\mathbf{R}^{k-\frac{1}{2}}$ is a matrix containing the inter-block diffusive transmissibility between blocks k and (k − 1) equal to

$$R_{ij}^{k-\frac{1}{2}} = \left(A\mathscr{D}_{ij}\right)^{k-\frac{1}{2}} \Big/ \left(0.5\Delta x^{k-1} + 0.5\Delta x^k\right), \tag{9}$$

where A^k and l^k are the cross-sectional area and length of grid block k, respectively.

We use upwinding based on the pressure gradient to estimate inter-block properties, where.

- If $P^{k-1} < P^k$, $\left(A\mathscr{D}_{ij}\right)^{k-\frac{1}{2}} = \left(A\mathscr{D}_{ij}\right)^k$,
- Otherwise, $\left(A\mathscr{D}_{ij}\right)^{k-\frac{1}{2}} = \left(A\mathscr{D}_{ij}\right)^{k-1}$.

This numerical model uses an explicit formulation, in which $\mathbf{f}^k$ is evaluated at time t in Eq. (8). The fracture is a boundary condition of constant composition $\mathbf{x}^f$ and pressure P^f of the injectant. Then, the flux at the boundary is

$$\Delta\mathbf{n} = \Delta t\mathbf{R}^f\left(\mathbf{f}^1 - \mathbf{f}^f\right), \tag{10}$$

where

$$R_{ij}^f = \mathscr{D}_{ij}^f (A/(0.5\Delta x))^1, \tag{11}$$

for i and j = 1, 2, …., N_C. $\mathscr{D}_{ij}^f$ is calculated for P^f and the injection composition $\mathbf{x}^f$ that is an infinite dilution of reservoir oil by the injectant.

D_{ij} is evaluated using the correlation of Leahy-Dios and Firoozabadi (2007) for infinite dilution coefficients and the Vignes mixing rules (Kooijman and Taylor, 1991), and with the LBC correlation (Lohrenz et al., 1964) for the viscosity of the mixture. The PR EOS is used to compute the pressure and fugacity from the molar volume and composition of the oil. The average pore size d needed for the Knudsen diffusion coefficient is computed using the Cozeny-Karman correlation

$$k = \varphi(d/2)^2 \Big/ 8\tau. \tag{12}$$

Appendix B validates the diffusion of multicomponent fluids through nanoporous media by using experimental data in the literature. It is important to note that Eq. (A2), which is used to evaluate $Đ_{iM}^e$ (i = 1,..,

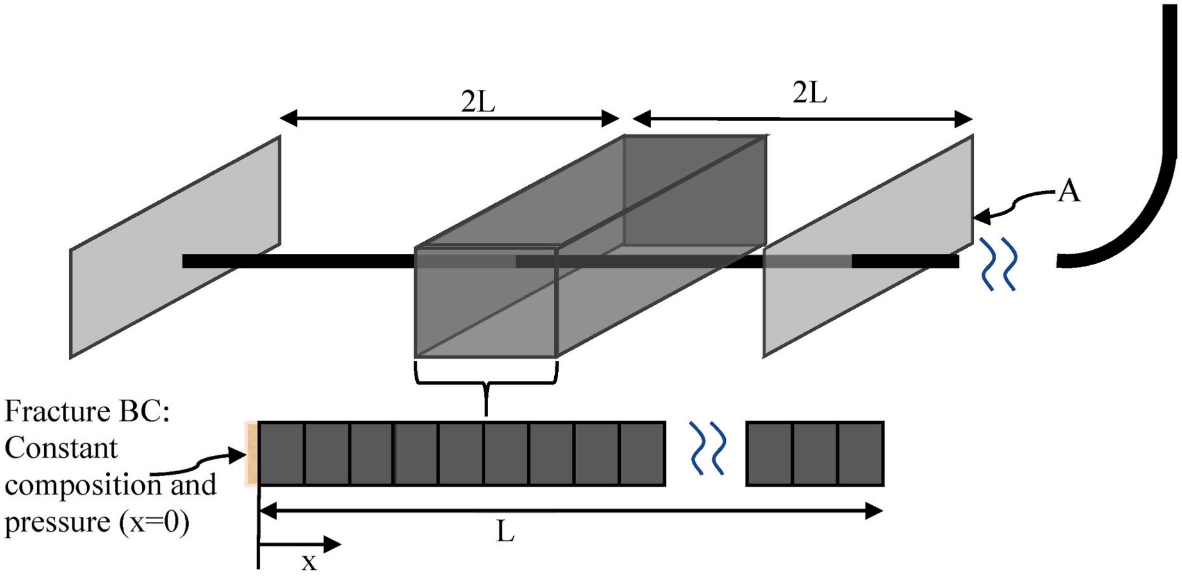

Fig. 1. Simplified schematic for a hydraulically fractured horizontal well. The fractures have a cross-sectional area A, and are separated by a distance equal to 2 L. The composition at the fracture is set as an infinite dilution of reservoir oil by the injectant. The discretized stencil is shown for the reservoir volume between the fracture and the half-distance between the two fractures. The matrix/fracture interface is located at x = 0 on the discretized stencil.

Nc), assumes that the fluid acts as a gas mixture of hard-spheres that only interact through collisions. This assumption ignores longer-distance interactions that cause the non-ideal behavior of fluid mixtures. As a result, we expect the value for the Knudsen diffusion coefficient $Đ_{iM}^{e}$ in a reservoir rock to be significantly smaller than the ones we used based on Eq. (A2). However, no model in the literature includes the effect of longer-distance interactions on non-ideal fluid behavior. Therefore, this paper focuses on identifying the parameters that define the relative sensitivity to pressure or injected solvent composition rather than making any analysis on the absolute magnitude of the rate of diffusion. The observations made in this paper have also been observed when $Đ_{iM}^{e}$ was multiplied by a factor of 10^{-3}.

3. Case studies

This section first presents the differences between the Maxwell-Stefan model and the new model developed in this research for multicomponent diffusive transport in tight porous media. Then, additional case studies give a detailed analysis of the main factors that influence the production rate through the multicomponent diffusion induced by miscible gas injection in tight reservoirs. A phase stability algorithm based on the minimization of the Helmholtz free energy (Achour and Okuno, 2020) is used to ensure that the hydrocarbon mixtures remain as a single phase throughout the simulation. Cases 1 and 2 use a simple ternary system. The main findings from case 2 are examined using a more realistic fluid system of six components in case 3. The Knudsen number is calculated to be greater than 0.1 for all cases, with which Knudsen diffusion is known to occur. As explained in the diffusion model section, the model presented in this paper is focused on single-phase diffusion. Hence, conclusions based on the case studies below are not made for more general conditions of mass transport in tight reservoirs.

3.1. Case 1. Maxwell-Stefan and dusty-gas models

This case compares the multicomponent diffusion simulated with the Maxwell-Stefan model with that with the dusty gas model for a tight formation. The initial mixture is 15% methane (C_1), 80% n-butane (nC_4), and 5% n-decane (nC_{10}) at 350 K and 400 bar. The injected solvent is pure C_1. Table 1 gives properties for the ternary system. The simulated 1-D domain is 9 m in length and discretized into 0.1-m grid-blocks (Table 2).

Fig. 2 shows the simulated profiles of pressure and molar volume after two years using the two models. The Maxwell-Stefan model only gives a net zero of local mass transfer. As a result, the molar volume profile is constant in time and space as shown by Fig. 1a. The increase in methane mole fraction at constant molar volume requires a substantial decrease in pressure in this case. The pressure gradient as a direct consequence of the Maxwell-Stefan model is inconsistent with its own assumption of no pressure gradient as explained in the Diffusion Models section. The assumption of no pressure gradient has been known as the mechanical equilibrium assumption (Taylor and Krishna, 1993). Although the Maxwell-Stefan model has been widely used, the self-inconsistency presented here is inherent and worth special attention to be paid in the context of shale EOR. Note that this inconsistency was found to persist even when Darcy's law is implemented with the permeability of 10 nD (Table 2).

In contrast, the new model allows for propagation of pressure gradients through Knudsen diffusion even under purely diffusive transport. Fig. 2b shows the pressure and molar volume profiles calculated by the new model developed in this research. The pressure profile is simulated to be nearly uniform after two years since non-zero net diffusion is allowed through Knudsen diffusion. The new model also keeps the internal consistency with its own assumptions, unlike the Maxwell-Stefan model.

Another issue that has been observed with the Maxwell-Stefan model is that numerical simulation can fail to converge when the constant molar volume assumed by the model cannot be met by varying composition during the simulation. This was observed, for example, when pure butane was injected to the reservoir composition 15% C_1, 30% nC_4, and 55% nC_{10} at 3000 bar and 350 K. After 44 days, the minimum allowable molar volume, given by the co-volume parameter in the cubic EOS, in the second grid block was $1.381187746 \times 10^{-4}\ m^3/mol$. However, the molar volume was $1.381187295 \times 10^{-4}\ m^3/mol$ as a result of the change in composition, which stopped the simulation from proceeding.

3.2. Case 2. ternary example for methane injection

The objective of this case is to mechanistically analyze the factors that can influence the isothermal multicomponent diffusion in tight porous media using a simple ternary system of methane (C_1), n-butane (nC_4), and n-decane (nC_{10}) given in Table 1. The injection fluid, 100% C_1, is at the fracture/matrix interface and diffused into the matrix that contains 15% C_1, 30% nC_4, and 55% nC_{10} at a given pressure and 300 K.

Diffusive paths were calculated at three pressures above the first contact miscibility pressure (FMP) as shown in Fig. 3 (a: 400 bar, b: 350 bar, and c: 300 bar). In all cases, nC_4 diffuses faster than nC_{10} toward the fracture, which causes the diffusive compositional paths to systematically deviate from the dilution line toward the nC_4-free binary edge. The compositions near the fracture are more time-dependent than those near the initial reservoir composition because the driving force for diffusion occurs from the fracture/matrix interface.

Unlike at 400 bar and 350 bar, the simulation at 300 bar was terminated when phase stability analysis indicated two phases in some grid blocks at 10.1 years as shown in Fig. 3c. Even though 300 bar is above the FMP defined by the isothermal-isobaric dilution line between the injection and initial reservoir compositions, the diffusive path calculated for this case goes through the two-phase region. Hence, the injection of solvent into a tight oil reservoir at a pressure above the FMP does not guarantee that only one phase exists in the reservoir during the diffusion process.

The diffusive path, however, seems to be only slightly time-dependent. Therefore, there exists a certain pressure at the fracture/matrix interface, above which the early-time composition path of the purely diffusive flow (with no convection) does not go through the two-phase region in composition-pressure space of isothermal multicomponent diffusion. This pressure, first-contact miscibility pressure of diffusion (FMP-D), should be above the traditionally defined FMP because of the faster diffusion of nC_4 than nC_{10} in this case. Khorsandi et al. (2014) derived an analytical solution for the composition path of a one-dimensional reservoir of incompressible fluid, including the effect of diffusion. As opposed to the current case, their solution shows that the

Table 1
Properties of components for Cases 1 and 2. Volume shift parameters are not used in this research because the volume shift concept is not generally applicable in tight reservoirs where equilibrium phases may have different pressures (Kumar and Okuno, 2015).

	Composition			Molecular weight	Critical temperature	Critical pressure	Acentric factor	Parachor	Critical density
	Case 1	Case 2	Solvent	g/mol	K	bar			g/cc
C_1	0.15	0.15	1	16.043	190.6	46	0.008	74.05	0.16169
nC_4	0.8	0.3	0	58.124	425.2	38	0.193	193.9	0.22801
nC_{10}	0.05	0.55	0	142.286	617.6	21.08	0.49	440.69	0.23648

Table 2

Properties of the one-dimensional porous medius for case 1.

φ	k mD	τ	A m^2	Δx m	N_{GB}	S_{wc}	γ	b_o	b_g	a_o	a_g	S_{omin}	S_{gmin}	Δt s
10%	10^{-5}	4	1	0.1	90	10%	3.88	0.386	−0.193	1	0.06	5%	5%	80

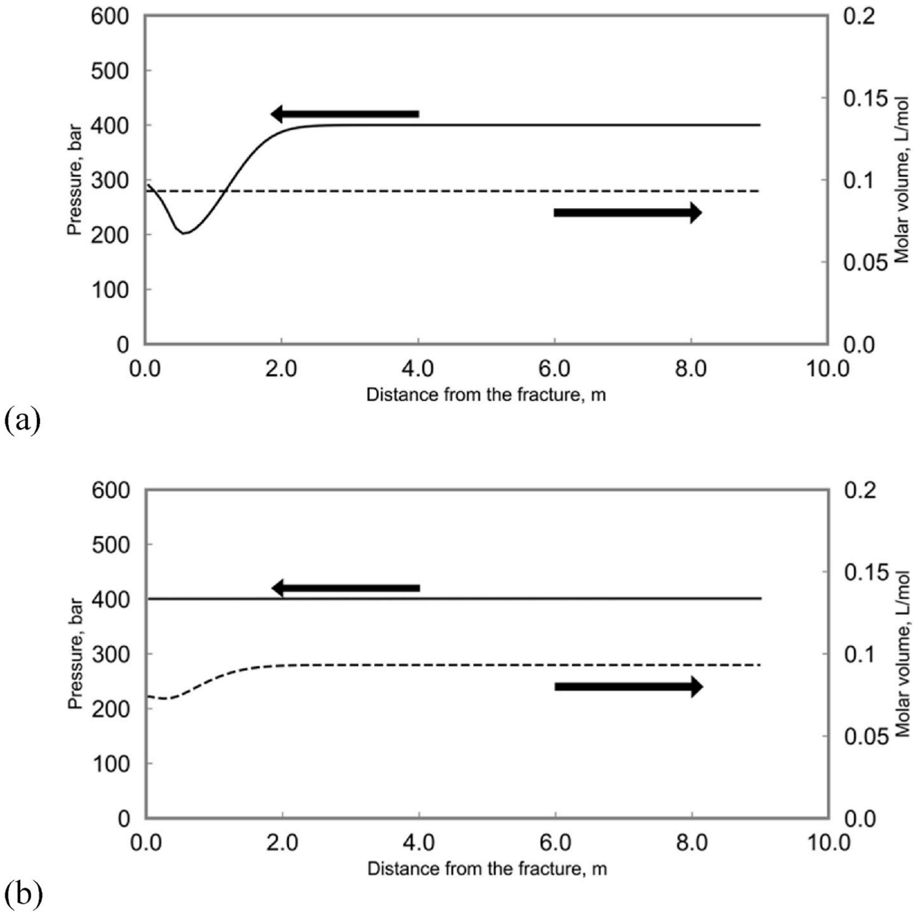

Fig. 2. Molar volume and pressure profile after two years of continuous methane injection calculated by using (a) the Maxwell-Stefan model and (b) the new model developed in this research. The reservoir initially contains 15% methane, 80% propane, and 5% n-decane at 350 K and 400 bar (Table 1).

composition path should be truly time-independent. The slight time independence observed here could be a numerical artifact resulting from the finite-difference discretization. In addition, the solution derived by Khorsandi et al. (2014) assumes both convection and diffusion with a constant flow velocity. This is different from constant-pressure injection through diffusion only, which is the process simulated in this case study.

Fig. 4 shows the molar recovery factors of nC_4 and nC_{10} at 300 bar, 350 bar, and 400 bar. The reason for the highest recovery simulated at 400 bar is explained below.

The diffusive flow rate is determined by $\dot{\boldsymbol{n}} = -c\mathbf{B}^{-1}(\boldsymbol{\varphi}P)^{-1}\nabla_T\mathbf{f}$ as shown in the previous section. The driving force is

$$\nabla_T\mathbf{f} \cong 2\left(\mathbf{x}^1\boldsymbol{\varphi}^1P^1 - \mathbf{x}^f\boldsymbol{\varphi}^fP^f\right) / \Delta x, \tag{13}$$

where the exponent "1" indicates the block adjacent to the fracture/matrix interface. The driving force for the injectant C_1 is generally negative $f^1_{C_1} - f^f_{C_1} < 0$, which drives methane into the matrix. Fig. 5a shows this driving force at the initial time (0 s), 1 h and 40 min, and 0.5 days. The magnitude of the driving force for C_1 decreases monotonically with time. The term that changes most between the three different pressure cases in the diffusion coefficient matrix is $(\boldsymbol{\varphi}P)^{-1}$, which decreases with increasing pressure. Therefore, the main factors that affect the production rates for the three different pressures are the driving force (Eq. (13)) and the term $(\boldsymbol{\varphi}P)^{-1}$ at $t = 0$. At $t = 0$, $P^1 = P^f$; that is, the driving force multiplied by $(\boldsymbol{\varphi}P)^{-1}$ for C_1 is written as $2(x^1_{C_1}\varphi^1_{C_1}/\varphi^f_{C_1} - 1)/\Delta x$. Table 3 shows that the ratio $\varphi^1_{C_1}/\varphi^f_{C_1}$ increases with increasing pressure, resulting in enhanced diffusive transport of C_1.

For nC_4 and nC_{10}, the driving force and its product with the $(\boldsymbol{\varphi}P)^{-1}$ term are positive since $x^f_{C_4}$ and $x^f_{C_{10}}$ are zero; i.e., $2x^1_{C_4}\varphi^1_{C_4}P^1/(\Delta x\varphi^f_{C_4}P^f) > 0$, and $2x^1_{C_{10}}\varphi^1_{C_{10}}P^1/(\Delta x\varphi^f_{C_{10}}P^f) > 0$. Fig. 5bc show that the driving force for nC_4 and nC_{10} increases first, and then decreases with time. Because the fugacities of nC_4 and nC_{10} for the fracture are 0 (their "fugacity coefficients" are not zero at the fracture), their driving force changes according to the pressures and fugacities of nC_4 and nC_{10} in the matrix. That is, this non-monotonic behavior with time (Fig. 5bc) is induced by the diffusion of C_1 into the matrix.

Fig. 6 shows the increase in pressure at early times for each case at the gridblock adjacent to the fracture. As C_1 starts to diffuse into the matrix, two factors affect the local pressure in the matrix: one is non-ideal mixing of components and the other is the relative diffusion rates of components as dictated by Eq. (8). Fig. 7 shows the pressure

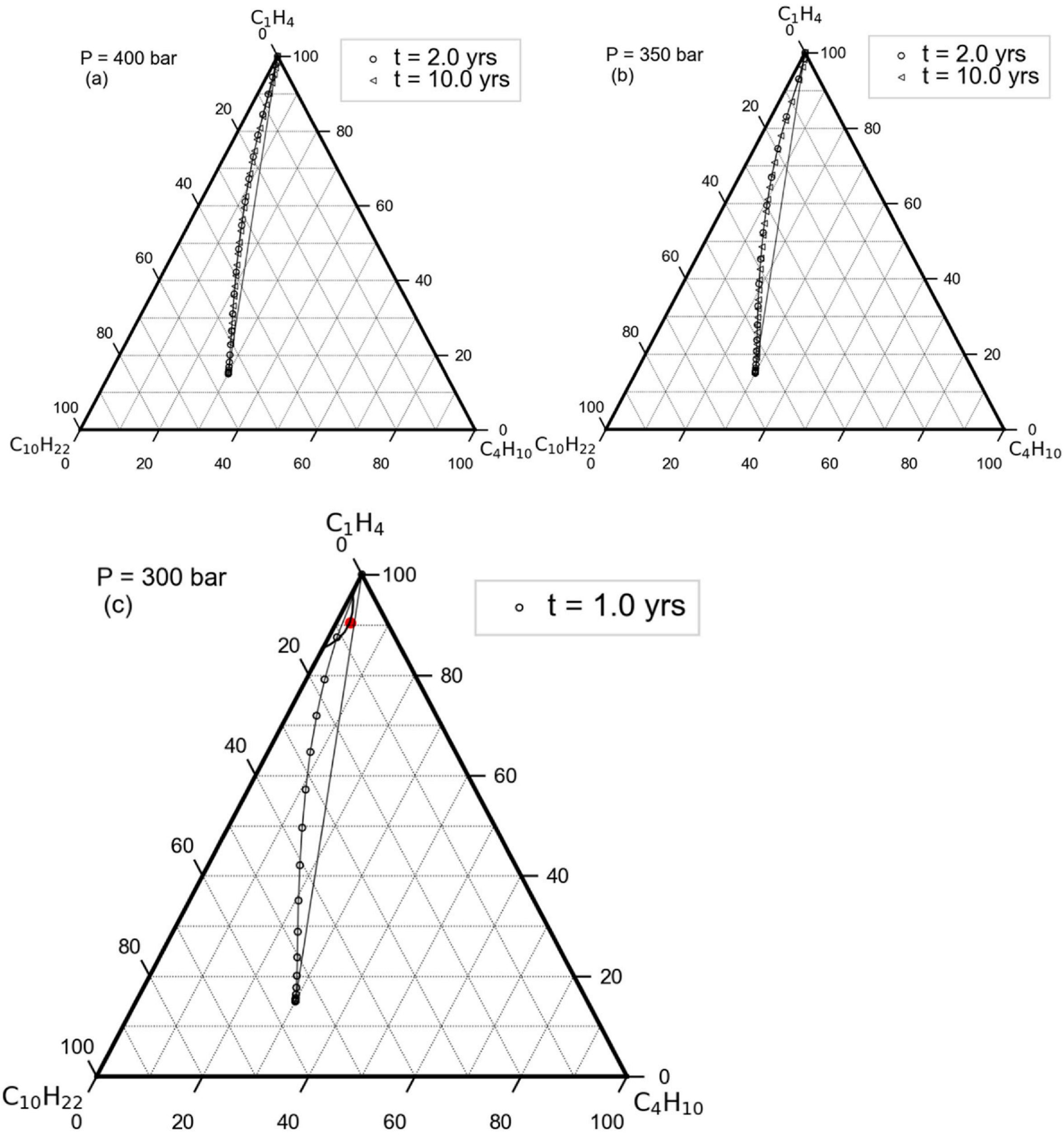

Fig. 3. Ternary diagrams representing the mixing path for methane injection into a hypothetical tight reservoir containing a mixture of methane, n-butane, and n-decane at (a) 400 bar, (b) 350 bar, and (c) 300 bar and 300 K. The mixing path for the 300-bar case is shown when the simulation was stopped because of the appearance of a second phase.

change upon mixing based on the PR EOS for the initial mixture with C_1 at a specified initial pressure. At low C_1 mole fractions, which are the domain of interest here, the pressure reduction upon mixing occurs to a similar extent for the three pressures tested. That is, the non-ideal mixing of components tends to reduce the driving force for diffusion of C_1 with increasing level of mixing of C_1 with the other components in this case.

The other factor affecting the local pressure in the matrix is related to the constraint given by Eq. (2). Eq. (2) can be rewritten as $\dot{n}_{C_1}/D^{e}_{C_1M} = -\dot{n}_{C_3}/D^{e}_{C_3M} - \dot{n}_{C_{10}}/D^{e}_{C_{10}M}$ at $t = 0$. The Knudsen diffusion coefficient is inversely proportional to the square root of the molecular weight of the component; therefore, C_1 diffuses into the matrix at a faster rate than the counter-current diffusion of propane and n-decane. This results in a higher rate of penetration of C_1 into the matrix relative to the production of nC_4 and nC_{10}. Fig. 8 shows the total number of moles for each component with respect to time. This figure clearly shows that the injection rate of methane dominates the total change of in-situ moles over that of nC_4 and nC_{10} for the 400-bar case. This leads to a substantial increase in pressure for the gridblock exposed to the fracture as shown in Fig. 6. The two competing factors described above determine the overall behavior of local pressures in the matrix.

Fig. 5c shows that the impact of this pressure increase on the driving force for nC_{10} becomes more significant as the initial pressure increases from 300 bar to 400 bar. This is because the fugacity coefficient of nC_{10} is more sensitive to pressure at higher pressures as shown in the last column of Table 3. The fugacity coefficient of nC_{10} increases by 0.0000288 from 300 bar to 350 bar, but it increases by 0.000039 from 350 bar to 400 bar. Moreover, Table 3 shows that the fugacity coefficient of nC_{10} nearly doubles from 300 bar to 400 bar, in contrast to the fugacity coefficient of nC_4 that only increases slightly with pressure. All these phenomena originate from the complex interplay among the components that is accounted for through the fugacity gradient as the

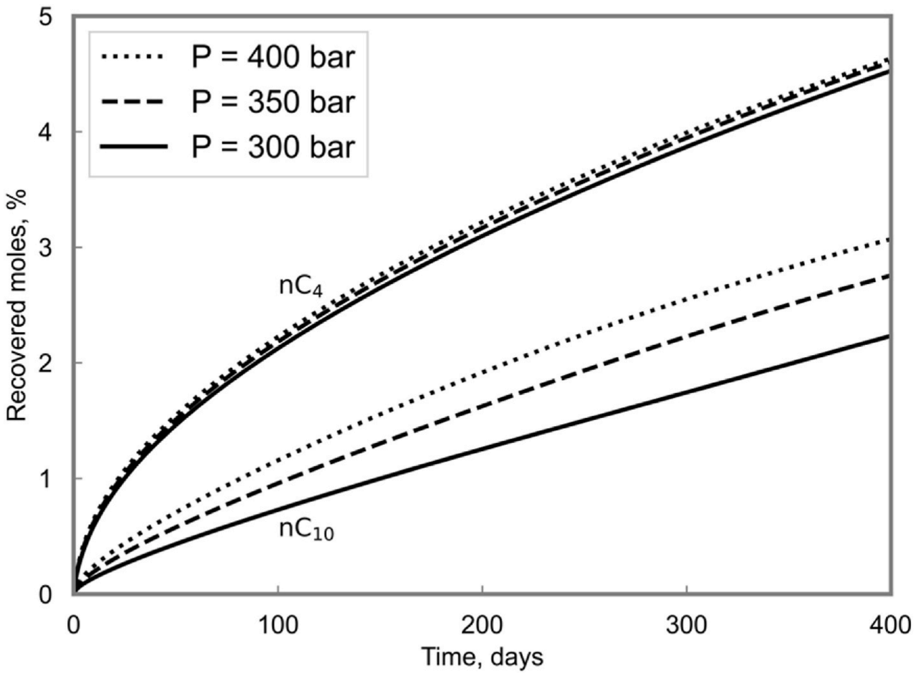

Fig. 4. Molar recovery factors for n-butane and n-decane simulated by using the new model for Case 1. Recovery of these components is simulated to be most efficient at 400 bars.

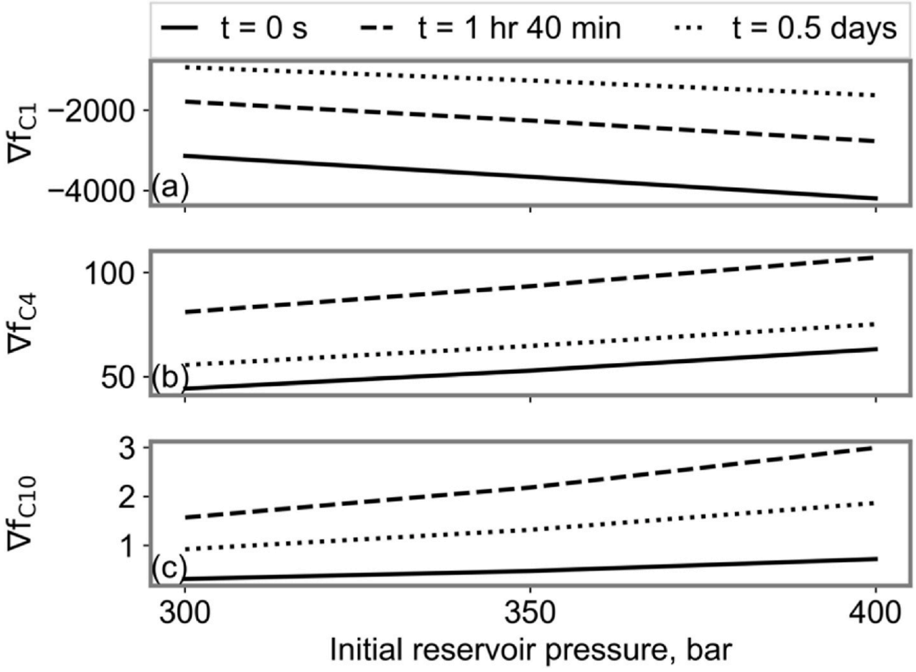

Fig. 5. Driving force at the fracture/matrix interface at early times for (a) C_1, (b) nC_4, and (c)nC_{10}. The driving force is shown at t = 0 s, t = 1 h and 40 min (corresponding to the maximum in pressure in Fig. 6), and t = 1 day. The y-axis is in bar/m.

driving force in the new model.

The late-time behavior is analyzed by $\dot{\boldsymbol{n}} = -c\mathcal{B}^{-1}(\boldsymbol{\varphi}P)^{-1}\nabla_T\mathbf{f}$ with the driving force depending on the properties of the fluid in the matrix. As pressure increases, the molar density c increases, which in turn increases the diffusive flux; however, this effect is suppressed by the normalization by the initial total moles. The elements of the diffusion coefficient matrix generally decrease with increasing pressure since they are correlated with pressure.

Figs. 9 and 10 show the profiles of the normalized driving force $(\boldsymbol{\varphi}P)^{-1}\nabla_T\mathbf{f}$ and composition after two days and after one year, respectively. After two days, the composition profiles are nearly identical for all three pressures. Although the driving force appears to respond mostly to the local composition, the magnitude of the normalized driving force at the fracture interface becomes greater with increasing injection pressure. At one year, the driving force has propagated from the fracture like a wave while keeping the relative differences in the normalized driving force among different pressures from early times. This causes a clear difference in the composition profiles after one year. Therefore, the

Table 3
Fugacity coefficients ratios and fugacity coefficients for C_1, nC_4, and nC_{10} at three different pressures at t = 0 for Case 2.

P	$\varphi^1_{C_1}/\varphi^f_{C_1}$	$\varphi^1_{C_4}/\varphi^f_{C_4}$	$\varphi^1_{C_{10}}/\varphi^f_{C_{10}}$	$\varphi^1_{C_1}$	$\varphi^1_{C_4}$	$\varphi^1_{C_{10}}$
Bar						
300	1.50	0.324	0.0484	1.01	0.0246	0.0000962
350	1.43	0.365	0.0717	0.955	0.0252	0.000125
400	1.38	0.401	0.0974	0.916	0.0263	0.000164

simulation results indicate that it would be important to design the diffusive oil recovery process by maximizing the early-time flux through the fracture/matrix interface so that it can yield a greater change in composition inside the matrix at later times. The supplementary material provides a sensitivity analysis for the 400-bar case.

3.3. Case 3. Eagle Ford oil with three different injectants

This case study presents simulation results for the production of an Eagle Ford light oil (Orangi et al., 2011) by the diffusion of miscible

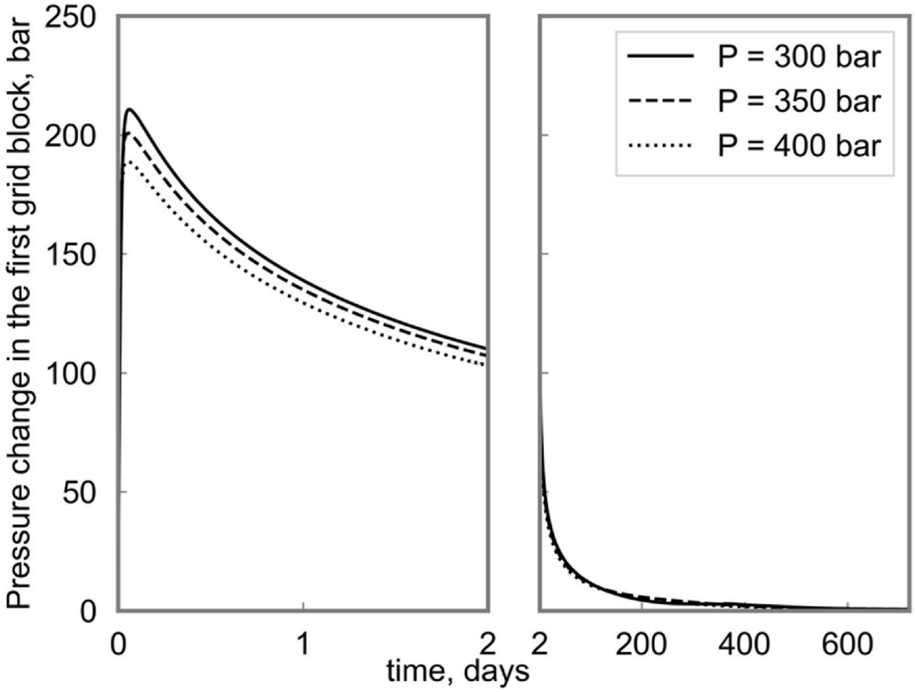

Fig. 6. Pressure of the gridblock adjacent to the fracture modeled by a constant pressure boundary condition for Case 2 at three different initial reservoir and injection pressures.

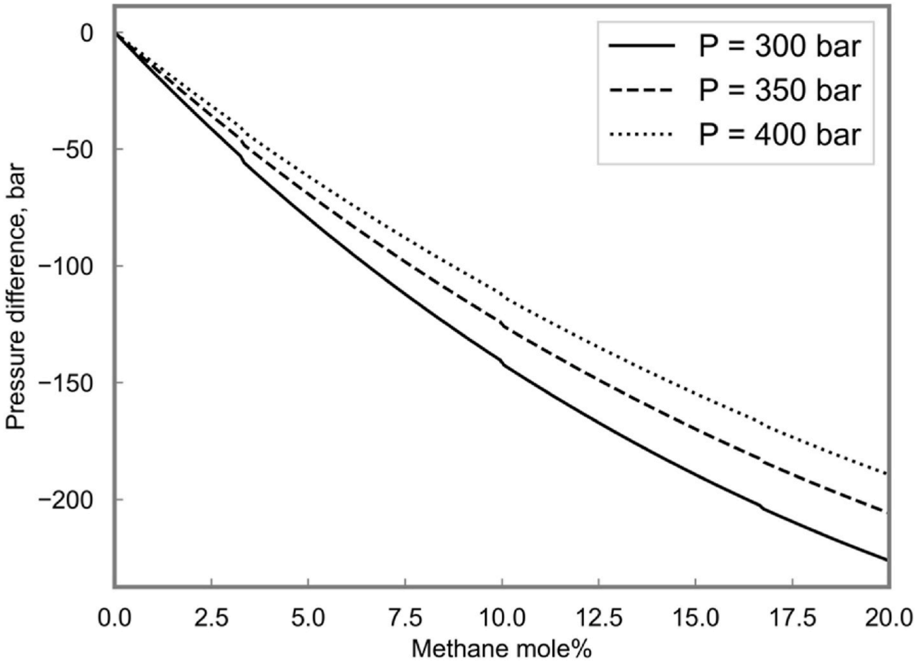

Fig. 7. Pressure change on mixing of the oil mixture in Case 2 with methane calculated at three different pressures by using the PR EOS (Table 1).

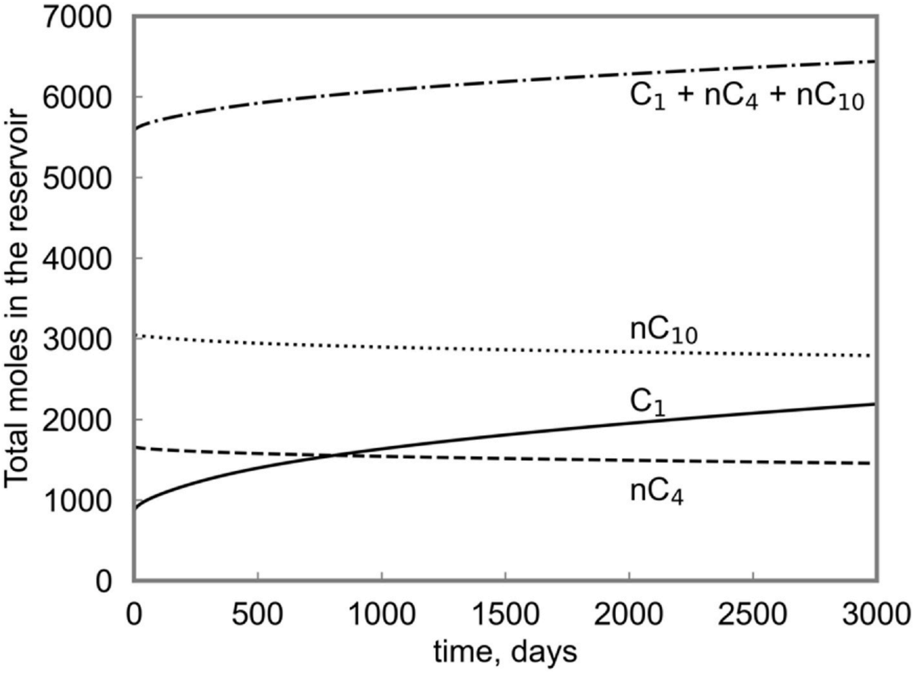

Fig. 8. Total number of moles for each component in the simulated reservoir for the 400-bar case.

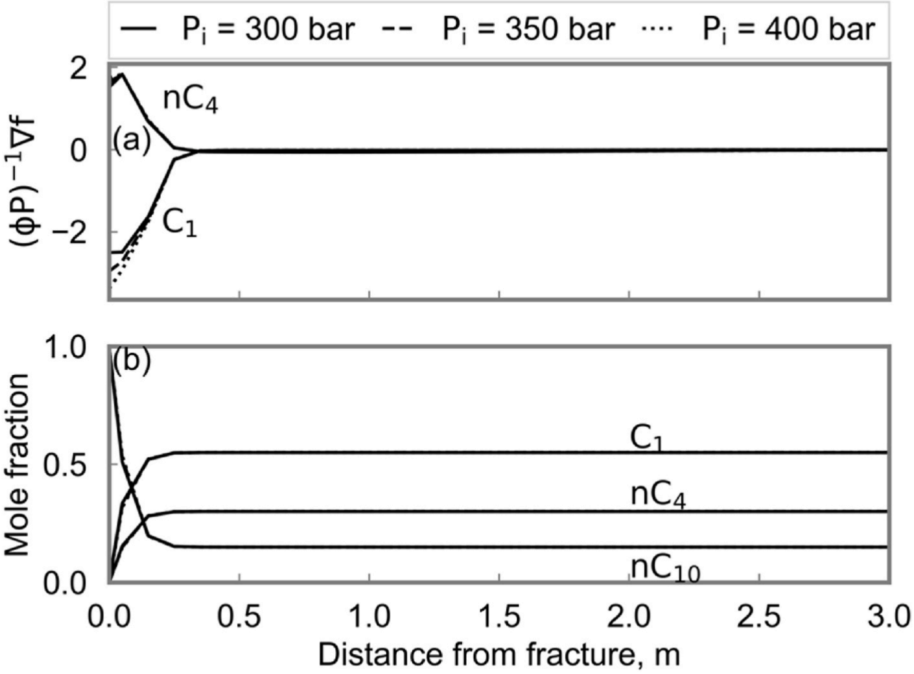

Fig. 9. Profiles at 2 days; (a) normalized driving force, and (b) composition. The driving force for nC_{10} is not shown because it is superposed with that of n-butane.

injection fluid from the fracture/matrix interface. Three injection fluids are considered: C_1, C_2, and CO_2. The parameters for the PR EOS are given in Tables 4 and 5.

Table 6 presents the properties of the one-dimensional porous media. The capillary pressure parameters, permeability, and porosity used to compute the capillary pressure in the stability analysis were taken from Neshat et al. (2020). Fig. 11 shows the Px diagram obtained from mixing the injectant and the Eagle ford light oil at 400 K including the effect of capillary pressure on phase boundaries (Achour and Okuno, 2020, 2021). It indicates that the highest FMP is 1000 bar for methane. To simulate the diffusive paths with no two-phase separation above FMP-D, the reservoir and injection pressure were set to be 2000 bar. The effect of two-phase separation is beyond the scope of this paper, and will be studied in a separate paper based on the recent development of phase-split calculation for tight reservoirs (Achour and Okuno, 2021).

Fig. 12 shows the recovery factors for the diffusion simulation for all non-solvent hydrocarbon components. For all components, the most efficient injectant for the production is C_1, followed by C_2, and finally by CO_2. The only difference among the three cases is the injection composition at the fracture/matrix interface for a given fracture/initial reservoir pressure. As discussed in Case 2, the key factor affecting the diffusion with the current formulation is the non-ideal interaction of

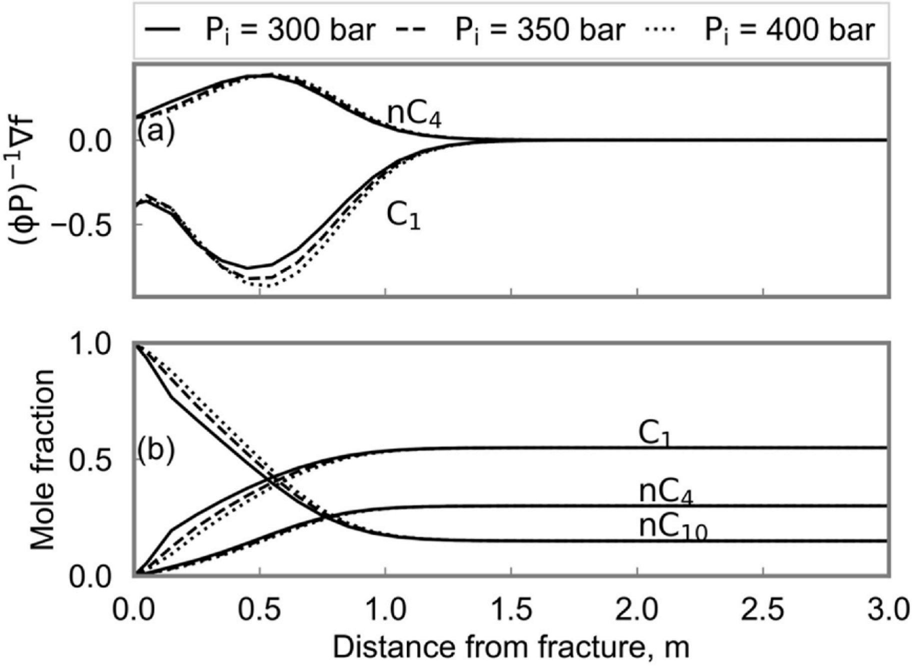

Fig. 10. Profiles at 1 year: (a) normalized driving force, and (b) composition. The driving force for nC_{10} is not shown because it is superposed with that of nC_4.

Table 4
PR EOS fluid model for an Eagle Ford light oil (Orangi et al., 2011) for Case 3.

	Composition mole fraction	Molecular weight g/mol	Critical pressure bar	Critical temperature K	Acentric factor	Parachor
N_2	0.00073	28.01	33.9349143	126.2	0.04	41
CO_2	0.01282	44.01	73.8431786	304.222222	0.225	78
C_1	0.31231	16.04	46.3944429	190.7	0.013	77.3
C_2	0.04314	30.07	48.8255536	305.427778	0.097	108.9
C_3	0.04148	44.1	42.5551214	369.888889	0.152	151.9
$i\text{-}C_4$	0.01350	58.12	36.46735	408.111111	0.185	181.5
$n\text{-}C_4$	0.03382	58.12	37.9562071	425.222222	0.201	191.7
$i\text{-}C_5$	0.01805	72.15	33.3269643	460.388889	0.2223	225
$n\text{-}C_5$	0.02141	72.15	33.7419143	469.783333	0.2539	233.9
$n\text{-}C_6$	0.04623	86.18	30.3078929	507.888889	0.3007	271
$C_{7\text{-}10}$	0.16297	112	27.7644286	589.166667	0.3739	311
$C_{11\text{-}14}$	0.12004	175	21.2093214	679.777778	0.526	471
$C_{15\text{-}19}$	0.10044	210	16.6393571	760.222222	0.6979	556.3
C_{20+}	0.07306	250	10.4151071	896.777778	1.0456	836.4

Table 5
Non-zero binary interaction parameters for the fluid shown in Table 4 (Orangi et al., 2011) for Case 3.

	N_2	CO_2	C_1	C_2	C_3	$i\text{-}C_4$	$n\text{-}C_4$	$i\text{-}C_5$	$n\text{-}C_5$
N_2	0								
CO_2	−0.02	0							
C_1	0.036	0.1	0						
C_2	0.05	0.13	0	0					
C_3	0.08	0.135	0	0	0				
$i\text{-}C_4$	0.095	0.13	0	0	0	0			
$n\text{-}C_4$	0.09	0.13	0	0	0	0	0		
$i\text{-}C_5$	0.095	0.125	0	0	0	0	0	0	
$n\text{-}C_5$	0.1	0.125	0	0	0	0	0	0	0
$n\text{-}C_6$	0.1	0.125	0	0	0	0	0	0	0
$C_{7\text{-}10}$	0.151	0.111	0.025	0.02	0.015	0.01	0.01	0.005	0.005
$C_{11\text{-}14}$	0.197	0.097	0.049	0.039	0.029	0.019	0.019	0.01	0.01
$C_{15\text{-}19}$	0.235	0.085	0.068	0.054	0.041	0.027	0.027	0.014	0.014
C_{20+}	0.288	0.07	0.094	0.075	0.056	0.038	0.038	0.019	0.019

components and their molecular weight, which cannot be satisfactorily modeled by the previous formulations. The non-ideal interaction of components is modeled through the fugacity coefficients and the pressure increase caused by non-ideal mixing in this research. This emphasizes the importance of calibrating the fluid model (the PR EOS in this research) with relevant experimental data for shale EOR.

Table 6
Parameters for the porous media used for Case 3.

φ	k mD	τ	A m^2	Δx m	N_{GB}	S_{wc}	γ	b_o	b_g	a_o	a_g	S_{omin}	S_{gmin}	Δt s
7%	10^{-5}	4	1	0.3	30	10%	3.88	0.386	−0.193	1	0.06	5%	5%	50

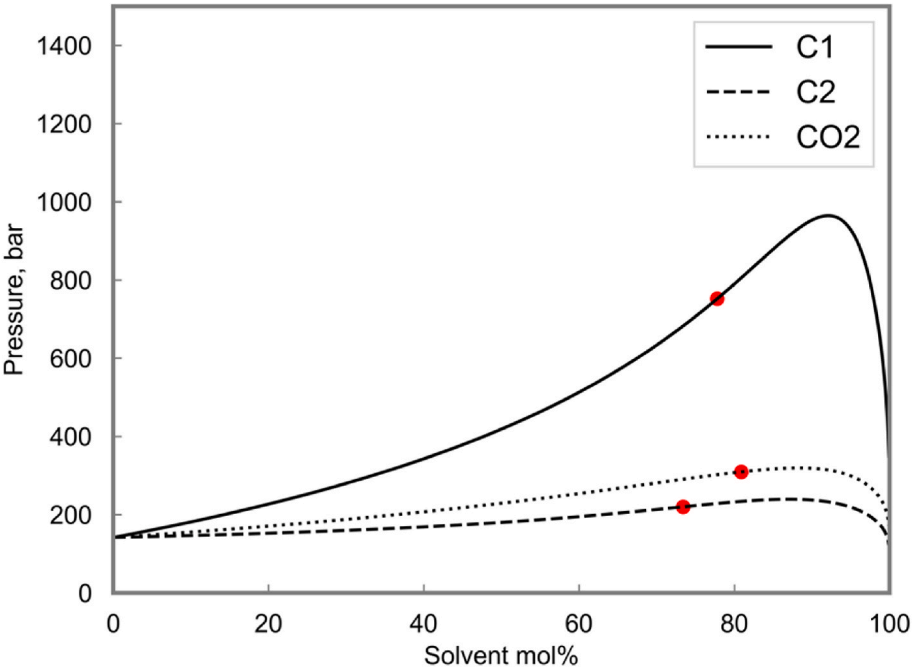

Fig. 11. Px diagrams for three injection fluids with the Eagle ford light oil at 400 K including the effect of capillary pressure for Case 3.

Fig. 13 shows the pressure increase simulated for each injectant. The CO_2 case results in the greatest pressure increase because it shows the most significant increase in pressure upon mixing as shown by the dotted line in Fig. 14. Table 7 shows the fugacity coefficients at 400 K and 2000 bar for an infinite dilution of the initial reservoir oil by the injectant (C_1, C_2, or CO_2). Even though CO_2 gives the highest pressure increase, the increased driving force is suppressed by a set of significantly greater fugacity coefficients than in the other two cases with C_1 and C_2. These higher fugacity coefficients cause a decrease in the matrix of diffusion coefficients at the fracture given by $\mathcal{D} = c\mathbf{B}^{-1}(\boldsymbol{\varphi}P)^{-1}$.

Ethane shows a higher pressure increase with non-ideal mixing effects than methane as shown by the dashed and solid lines in Fig. 14. However, the molecular weight of methane is smaller than ethane by a factor of almost two. These two competing factors lead to a greater pressure increase when methane is injected as a solvent than ethane as shown in Fig. 13. Table 7 shows that the fugacity coefficients of the oil components at infinite dilution in the injectant are higher for methane as the injectant than ethane as predicted by the PR EOS [the PR EOS has been found accurate for the purpose when fitted to the data by Debenedetti and Kumar (1986) and Ahlers and Gmehling (2002)]. This difference is more pronounced for lighter components than heavier ones. This difference in fugacity coefficients combined with the difference in pressure increase between the two solvents yields higher recovery factors for lighter components when methane is used as a solvent and approximately equal for heavier ones.

Note that the relative performance of the solvents considered in this case study depends on the characterized EOS model, oil composition, temperature, and pressure of the reservoir. Therefore, the relative performance of solvents in this case study should not be taken as a general result. This analysis provides how the relative performance of solvents can be affected by the pressure change on mixing and the diffusion coefficient for the oil components in the solvent at infinite dilution. The relative performance of the solvents may deviate from the observations above if diffusion were coupled with other physical phenomena. For example, 1) if the initial reservoir pressure were 500 bar, methane injection would result in the appearance of a gaseous phase, which could allow the solvent to penetrate further into the reservoir, enhance the mixing with the oil, and increase counter-current diffusion of other hydrocarbon molecules; 2) the inclusion of convective flow would further increase the rate of oil production for CO_2 because the pressure increase on mixing would create a pressure gradient; 3) the inclusion of sorption could slow down the rate of diffusion of heavier hydrocarbons for all cases as molecular dynamics simulation showed that heavier hydrocarbons tended to adsorb more strongly to solid organic matter in the pore space (Wang et al., 2015).

4. Conclusions

This paper presents a new formulation of multicomponent diffusive transport in tight porous media based on the assumptions of no convective flow and no external forces. The non-ideal interactions among all components of the injection and initial reservoir fluids are properly considered in the formulation. The fluid non-ideality is modeled through not only the component fugacities, but also the volume change on mixing that causes local pressures to change under low permeability. The dusty gas model allows for non-zero net diffusion causing an additional compositional effect on multicomponent diffusion.

- The importance of fugacity coefficients and volume change on mixing was observed in the case studies. These two factors represent fluid non-ideality and collectively affect the driving force of

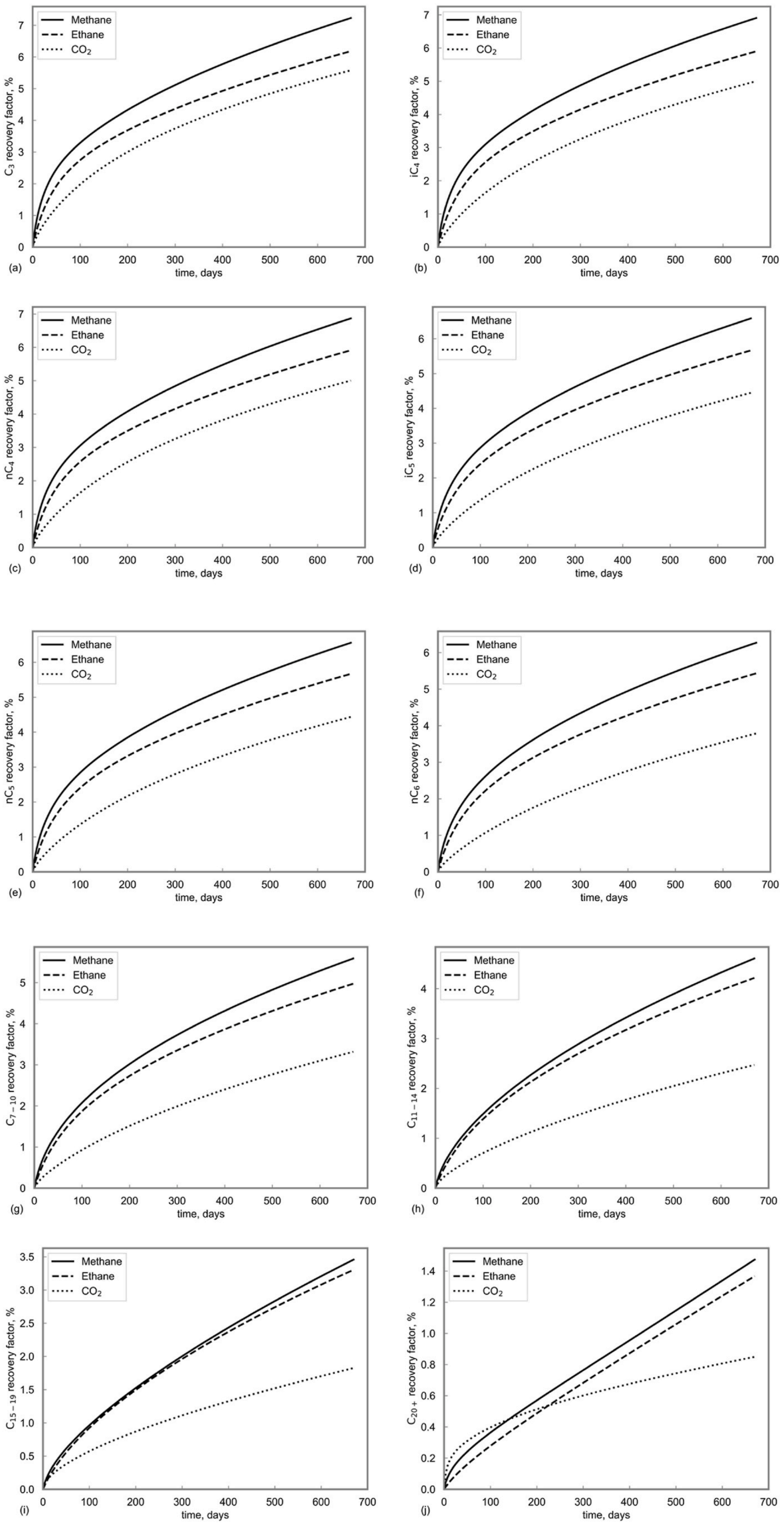

Fig. 12. Recovery factors for each non-solvent hydrocarbon component when three different solvents are injected in Case 3.

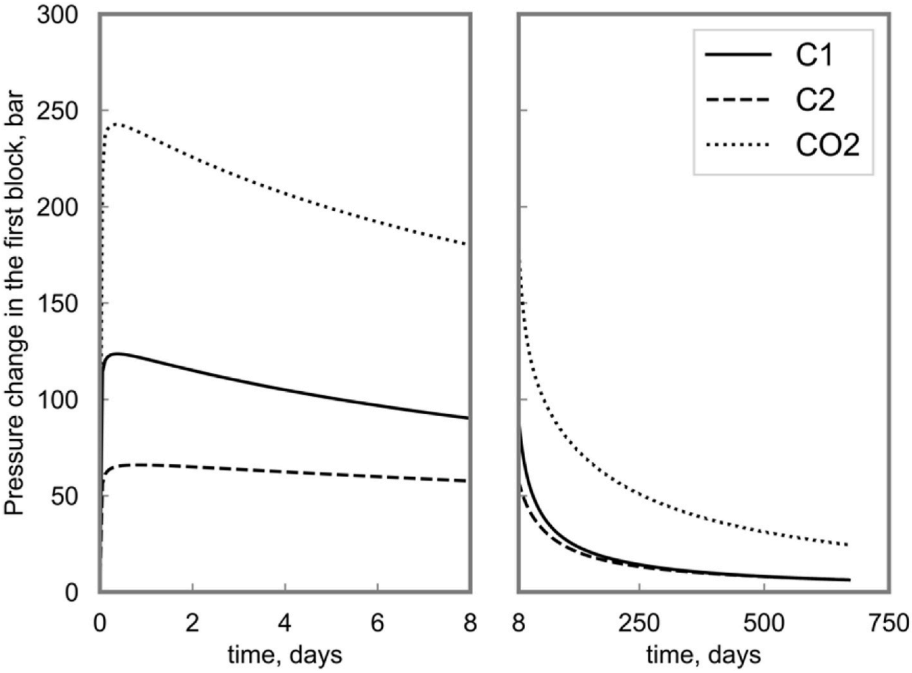

Fig. 13. Pressure of the grid block directly adjacent to the fracture when three different solvents are injected into an Eagle Ford light oil reservoir in Case 3.

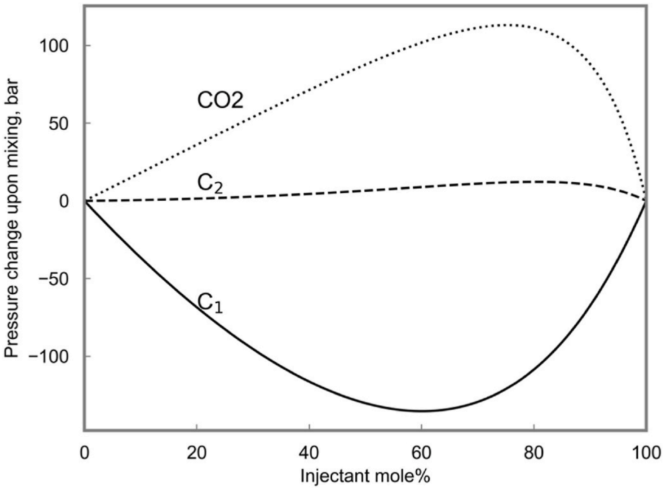

Fig. 14. Pressure change upon mixing of Eagle Ford light oil with three different solvents at 2000 bar and 400 K.

Table 7

Fugacity coefficients at 400 K and 2000 bar for an infinite dilution of reservoir oil by the injectant, CO_2, C_1, or C_2 for case 3.

Solvent	CO_2	C_1	C_2
N_2	4.715	3.470	4.480
CO_2	0.971	1.422	1.478
C_1	3.192	2.141	2.293
C_2	3.088	1.870	1.699
C_3	4.440	2.304	1.934
iC_4	7.771	3.475	2.854
nC_4	6.243	2.920	2.275
iC_5	11.165	4.523	3.453
nC_5	9.982	4.132	3.050
nC_6	17.974	6.216	4.400
$C_{7\text{-}10}$	22.60	10.18	6.053
$C_{11\text{-}14}$	173.1	85.38	45.50
$C_{15\text{-}19}$	2467.	1515.	733.3
C_{20+}	$3.953\ 10^7$	$2.931\ 10^7$	$1.637\ 10^7$

multicomponent diffusion. The non-ideal interaction of components should be properly characterized and utilized to enhance the early-time flux through the fracture/matrix interface in miscible EOR in tight reservoirs.

- The Maxwell-Stefan model was found to be inconsistent with its own assumption of no pressure gradient when non-ideal mixing is considered for tight reservoirs. The dusty gas model does not have this issue by allowing for pressure gradients to drive the mass transfer by Knudsen diffusion.
- Case studies identified two main factors influencing the oil production rate during the diffusion of the miscible injectant; that is, the local pressure change because of the volume change on mixing, and the fugacity coefficients for the injectant and reservoir oil. In addition to the thermodynamic factors, the pressure change is also affected by the Knudsen diffusion that yields more rapid transfer of smaller molecules. These findings indicate the importance of calibrating the EOS fluid model with relevant experimental data for shale EOR.
- Injection of solvent into a tight oil reservoir at a pressure above the traditionally defined first-contact-miscible pressure (FMP) does not guarantee that only one hydrocarbon phase exists in the reservoir during the diffusion process. A first-contact miscibility pressure of diffusion (FMP-D) is generally different from FMP. In the ternary case (Case 1), FMP-D was greater than FMP because of the faster diffusion of nC_4 than nC_{10} when C_1 was diffused into the matrix.

Declaration of competing interest

The authors declare that they have no known competing financial interests or personal relationships that could have appeared to influence the work reported in this paper.

Acknowledgment

Ryosuke Okuno holds the Pioneer Corporation Faculty Fellowship in Petroleum Engineering at The University of Texas at Austin.

Nomenclature

Roman symbols

A	Cross-sectional area
a_o	Capillary pressure parameter for capillary pressure correlation of Neshat et al. (2018)
a_g	Capillary pressure parameter for capillary pressure correlation of Neshat et al. (2018)
b_o	Capillary pressure parameter for capillary pressure correlation of Neshat et al. (2018)
b_g	Capillary pressure parameter for capillary pressure correlation of Neshat et al. (2018)
$\mathcal{B}$	Matrix containing the inverse of diffusion coefficients defined in the Diffusion models section
$\mathbf{B}$	Matrix containing the inverse of diffusion coefficients defined in the Appendix A
c	Molar density
c_i	Molar density of component i
d	Average pore diameter calculated with Eq. (9)
$\boldsymbol{D}$	Matrix containing diffusion coefficients for generalized Fick's law
D	Diffusion coefficient used with the classical Fick's law
$\mathcal{D}$	Matrix containing fugacity-based diffusion coefficients
$\mathscr{D}_{ij}$	Binary diffusion coefficient for pair i and j
Đ_{ij}	Binary diffusion coefficients for binary pair i and j
Đ^{e}_{ij}	Effective binary diffusion coefficients for binary pair i and j
Đ^{e}_{iM}	Effective Knudsen diffusion coefficients for component i defined by Eq. (A2)
$\mathscr{F}$	Faraday's constant
f_i	Fugacity of component i
$\mathbf{f}$	Vector containing the fugacities of each component in a mixture
J_j	Net diffusive flux for component i
k	Permeability of a porous medium
l	Grid-block length
M_i	Molecular weight of component i
N_c	Number of components
N_{GB}	Number of grid blocks
$\dot{n}_i$	Molar flux of component i
$\dot{\boldsymbol{n}}$	Vector containing molar fluxes for each component
$\mathbf{n}$	Vector containing number of moles of each component in a grid block
P	Pressure
R	Ideal gas constant
$\mathbf{R}^{k-\frac{1}{2}}$	Matrix containing the diffusive transmissibility between block k and block k-1defined by Eq. (6)
R_{ij}	Diffusive transmissibility matrix for binary pair i and j
S_{wc}	Connate water saturation
S_{omin}	Capillary pressure parameters used in the stability analysis (Achour and Okuno, 2020)
S_{gmin}	Capillary pressure parameters used in the stability analysis (Achour and Okuno, 2020)
T	Temperature or equation for the tangent plane to a surface
$\underline{V}$	Molar volume
$\overline{V}_i$	Partial molar volume for component i
x	Distance; grid block width when used as "Δx"
x_i	Mole fraction for component i
$\mathbf{x}$	Vector containing component mole fractions in a mixture
z_i	Electrostatic charge of component i

Greek letters

α_i'	Modified viscous selectivity factor for component i (Krishna and Wesselingh, 1997)
η	Viscosity
γ	Parachor exponent used to calculate the interfacial tension
γ	Activity coefficient defined by Eq. (A4)
γ'	Derivative of γ with respect to molar density
$\boldsymbol{\Gamma}$	Matrix containing the elements $x_i \partial \ln f_i / \partial x_j$ $(i = 1, \ldots, N_c - 1; j = 1, \ldots, N_c - 1)$
μ_i	Chemical potential for component i
φ_i	Fugacity coefficient for component i
$\boldsymbol{\varphi}$	Diagonal matrix containing the fugacity coefficient for each component in its diagonal
φ	Porosity of a porous medium
Φ	Electrostatic potential
τ	Tortuosity

Superscripts

e	Effective value for porous medium
f	Fracture modeled by a boundary condition of constant composition and pressure
k	Index for grid block

Subscripts

T	Constant temperature
P	Constant pressure

Abbreviations

BC	Boundary condition
FMP	First-contact miscibility pressure
FMP-D	First-contact miscibility pressure of diffusion
EOR	Enhanced oil recovery
PR EOS	Peng-Robinson (1978) equation of state

Appendix C. Supplementary data

Supplementary data to this article can be found online at https://doi.org/10.1016/j.petrol.2022.110469.

Appendix A

The dusty gas model is one of the most general diffusion models for multicomponent mixtures through a porous media based on continuum physics (Mason and Malinauskas, 1983; Krishna and Wesselingh, 1997). It formulates the molecular diffusion and Knudsen diffusion driven by the isothermal chemical potential gradient $\nabla_T \mu_i$ and external forces, such as electrostatic potential gradient $\nabla \Phi$. The most general form that includes the effect of viscous forces is given by

$$-\frac{x_i}{RT}\nabla_{T,P}\mu_i - \frac{x_i \overline{V}_i}{RT}\nabla P - \frac{\alpha_i' x_i k}{\text{Đ}_{iM}\eta}\nabla P - \frac{z_i \mathscr{F}}{RT}\nabla \Phi = \underline{V}\sum_{\substack{j=1 \\ j\neq i}}^{N_c}\frac{x_j \dot{n}_i - x_i \dot{n}_j}{\text{Đ}_{ij}^e} + \underline{V}\frac{\dot{n}_i}{\text{Đ}_{iM}^e}, \tag{A1}$$

for all components $i = 1, 2, \ldots, N_c$, where R is the universal gas constant, T is temperature, P is pressure, $\mathscr{F}$ is Faraday's constant units of temperature per mole, and η is the viscosity of the mixture. In Eq. (A1), x_i, $\overline{V}_i$, z_i, α_i', D_{iM}^e, and $\dot{n}_i$ are the mole fraction, the partial molar volume, the electrostatic charge, the dimensionless modified selective diffusivity factor, the effective Knudsen diffusion coefficient, and the molar flux of component i, respectively. The effective diffusion coefficients in porous media are calculated from bulk diffusion measurements as $D_{ij}^e = D_{ij}\varphi/\tau$, where φ is the porosity, τ is the tortuosity, and D_{ij} is the effective bulk diffusivity for the ij binary pair. The effective Knudsen diffusivity (Krishna and Wesselingh, 1997) is defined as

$$\text{Đ}_{iM}^e = (\varphi / \tau)(d\ / 3)\sqrt{8RT/\pi M_i}, \tag{A2}$$

where $i = 1, 2, \ldots, N_c$, d is the average pore size, and M_i is the molecular weight of component i.

Several studies used various assumptions that simplified Eq. (A1) to model the mass transport through tight porous media. The most widely used form of the Maxwell-Stefan diffusion model can be obtained from the dusty gas model by neglecting viscous flow, electrostatic potential, and Knudsen diffusion as follows:

$$-\frac{x_i}{RT}\nabla_{T,P}\mu_i - \frac{x_i \overline{V}_i}{RT}\nabla P = \underline{V}\sum_{\substack{j=1 \\ j\neq i}}^{N_c}\frac{x_j J_i - x_i J_j}{\text{Đ}_{ij}^e}, \tag{A3}$$

where $i = 1, 2, \ldots, N_c$, and J_i is the net diffusive flux of component i. The implicit assumption of mechanical equilibrium $\nabla P = 0$ results from taking the summation of Eq. (A3) for the N_C components and using the Gibbs-Duhem relation (Taylor and Krishna, 1993). The internal consistency on this assumption requires no effect of the pressure gradient on the chemical potential gradient; hence, the pressure gradient term in Eq. (A3) should be dropped as is often done.

Alharthy et al. (2018) and Hoteit (2013) used the generalized Fick's law based upon the Maxwell-Stefan equation, in which the flow was driven by the concentration gradient $\mathbf{J} = -\underline{V}^{-1}\boldsymbol{D}\nabla\mathbf{x}$. $\boldsymbol{D}$ is a $(Nc - 1) \times (Nc - 1)$ matrix of generalized diffusion coefficients defined as $\boldsymbol{D} = \mathbf{B}^{-1}\boldsymbol{\Gamma}$, where $\Gamma_{ij} = x_i \partial \ln f_i / \partial x_j$ $(i,j = 1, 2, \ldots, N_c - 1)$, and the non-diagonal elements of matrix $\mathbf{B}$ are $B_{ij} = -x_i(1/\text{Đ}_{ij} - 1/\text{Đ}_{iN_c})$ for i and $j = 1, 2, \ldots, N_C - 1$ and the diagonal elements are $B_{ii} = x_i/\text{Đ}_{iN_c} + \sum_{\substack{k=1 \\ k\neq i}}^{N_c} x_k/\text{Đ}_{ik}$ for $i = 1, 2, \ldots, N_C - 1$.

Another commonly used form of Eq. (A1) can be derived by assuming that the chemical potential is of the form (Bothe, 2011)

$$\mu_i = \mu_{i0} + RT\ln(\gamma c_i) \tag{A4}$$

for a binary mixture, where c_i is the molar density of component i, and γ is a function of molar density. Neglecting Knudsen diffusion, viscous flow, and external forces, Eq. (A1) and (A4) give Fick's law of diffusion:

$$J_1 = -Đ^e_{12}(1 + c\gamma' / \gamma)\nabla c = -D\nabla c. \tag{A5}$$

This form was used by Cronin et al. (2019) with a constant D to simulate the diffusive transport of solvent into a tight matrix. The most commonly used form of Fick's law can be derived directly from Eq. (A3) assuming that the fluid mixture is an ideal solution

$$J_1 = -Đ^e_{12}\nabla x_1 \tag{A6}$$

for $i = 1, \ldots, N_c$.

The models presented above are based on reasonable assumptions for fluid flow through tight porous media, such as negligible viscous flow and negligible external forces. One of the assumptions that are questionable for tight reservoir conditions under enhanced oil recovery is a negligible pressure gradient in the Maxwell-Stefan diffusion, which does not allow for the non-ideal mixing of components. Also, the first form of Fick's law (Eq. (A5)) assumes a constant factor of $1 + c\gamma'/\gamma$. The second form of Fick's law is based on ideal solution, which is only valid at low temperatures (Sandler, 2017).

Appendix B

This section validates the diffusion simulation model using experimentally measured rates of diffusion for multiple ternary mixtures of N_2, H_2, He, and Ar across nanoporous plugs as measured by Šolcová et al. (2001). The artificial nanoporous core plugs were made of inert materials to ensure that sorption and surface diffusion did not occur and only diffusion took place. The gases at both ends of the core plugs were kept at a constant composition and at equal pressure to suppress viscous displacement. The bottom boundary condition was set to pure helium at a constant pressure while the top boundary was a binary mixture at a constant composition made of nitrogen-hydrogen, argon-hydrogen, or argon-nitrogen for varying mole fractions of nitrogen, argon, and argon, respectively, as shown in Fig. B-1. This figure shows the experimental data by hollow triangles, circles, and squares while the simulated flow rates by solid, dashed, and dotted lines for Nitrogen–Hydrogen, Argon–Hydrogen, and Argon–Nitrogen mixtures, respectively. This plot shows that there is a noticeable gap between the measured net diffusion rate and the simulated one at equilibrium. This is expected since the Peng-Robinson (1978) equation of state model used is not optimized for non-hydrocarbon gases at low pressures. Table B-1 shows the parameters for this equation of state model. However, the simulation model computes quantitatively reasonable trends for the diffusion fluxes through nanoporous media. This allows us to use an equation of state that is calibrated at reservoir conditions to estimate the diffusion rates at those conditions.

Table B- 1
Properties of components for the experimental validation. These parameters were taken from Poling et al. (2001).

	Molecular weight g/mol	Critical temperature K	Critical pressure bar	Acentric factor	Critical density g/cc
He	4.003	5.19	2.27	−0.39	0.16169
N_2	28.04	126.2	33.98	0.037	0.22801
H_2	2.016	33.25	12.97	−0.216	0.23648
Ar	39.948	150.86	49.98	−0.002	0.53571

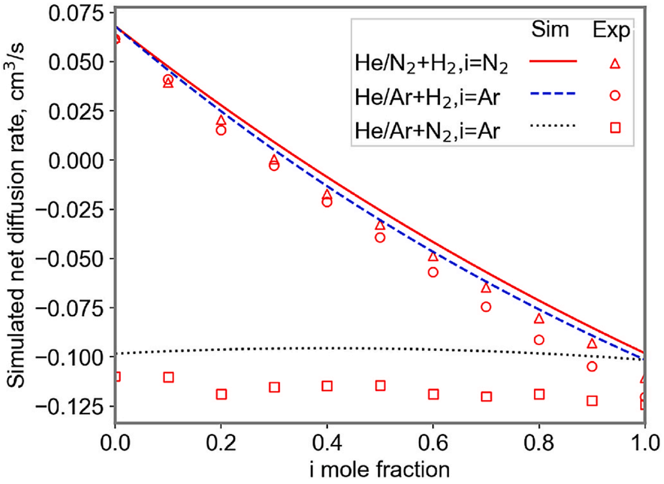

Fig. B-1. Comparison of experimentally measured diffusion fluxes for three ternary mixtures with the simulated values at atmospheric pressure and temperature. The x-axis indicates the mole fraction of component i in the binary mixture as indicated in the legend.

References

Achour, S.H., Okuno, R., 2020. Phase stability analysis for tight porous media by minimization of the Helmholtz free energy. Fluid Phase Equil. 520, 112648. https://doi.org/10.1016/j.fluid.2020.112648.

Achour, S.H., Okuno, R., 2021. Two-phase flash for tight porous media by minimization of the Helmholtz free energy. Fluid Phase Equil. 534, 112960. https://doi.org/10.1016/j.fluid.2021.112960.

Afsharpoor, A., Javadpour, F., 2016. Liquid slip flow in a network of shale noncircular nanopores. Fuel 180, 580–590, 10.1016/j.fuel.2016.04.078.

Ahlers, J., Gmehling, J., 2002. Development of a universal group contribution equation of state III. Prediction of vapor−liquid equilibria, excess enthalpies, and activity coefficients at infinite dilution with the VTPR model. Ind. Eng. Chem. Res. 41 (23), 5890–5899. https://doi.org/10.1021/ie0203734.

Alharthy, N., Teklu, T.W., Kazemi, H., Graves, R., Hawthorne, S., Braunberger, J., Kurtoglu, B., 2018. Enhanced oil recovery in liquid-rich shale reservoirs: laboratory to field. SPE Reservoir Eval. Eng. 21 (1), 137–159, 10.2118/175034-PA.

Babaei, M., Mu, J., Masters, A.J., 2018. Impact of variation in multicomponent diffusion coefficients and salinity in CO2-EOR: a numerical study using molecular dynamics simulation. J. Petrol. Sci. Eng. 162, 685–696. https://doi.org/10.1016/j.petrol.2017.10.086.

Bhatia, S.K., Bonilla, M.R., Nicholson, D., 2011. Molecular transport in nanopores: a theoretical perspective. Phys. Chem. Chem. Phys. 13 (34), 15350–15383. https://doi.org/10.1039/C1CP21166H.

Bothe, D., 2011. On the Maxwell-Stefan approach to multicomponent diffusion. Parabol. Prob. 80, 80–93. https://doi.org/10.1007/978-3-0348-0075-4_5.

Burrows, L.C., Haeri, F., Cvetic, 2020. A literature review of CO2, natural gas, and water-based fluids for enhanced oil recovery in unconventional reservoirs. P Energy Fuels 34 (5), 5331–5380. https://doi.org/10.1021/acs.energyfuels.9b03658.

Cihan, A., Tokunaga, T.K., Birkholzer, J.T., 2019. Adsorption and capillary condensation-induced imbibition in nanoporous media. Langmuir 35 (29), 9611–9621. https://doi.org/10.1021/acs.langmuir.9b00813.

Cronin, M., Emami-Meybodi, H., Johns, R.T., 2019. Diffusion-dominated proxy model for solvent injection in ultratight oil reservoirs. SPE J. 24 (2), 660–680. https://doi.org/10.2118/190305-PA.

Cronin, M., Emami-Meybodi, H., Johns, R.T., 2021. Multicomponent diffusion modeling of cyclic solvent injection in ultratight reservoirs. SPE J. 26 (3), 1213–1232, 10.2118/196008-PA.

Debenedetti, P.G., Kumar, S.K., 1986. Infinite dilution fugacity coefficients and the general behavior of dilute binary systems. AIChE J. 32 (8), 1253–1262, 10.1002/aic.690320804.

Hoteit, H., 2013. Modeling diffusion and gas–oil mass transfer in fractured reservoirs. J. Petrol. Sci. Eng. 105, 1–17. https://doi.org/10.1016/j.petrol.2013.03.007.

Hoteit, H., Firoozabadi, A., 2009. Numerical modeling of diffusion in fractured media for gas injection and recycling schemes. SPE J. 14 (2), 323–337. https://doi.org/10.2118/103292-PA.

Imai, M., Sumikawa, I., Yamada, T., Nakano, M., 2012. Reservoir fluid characterization for tight fractured reservoirs: effect of diffusion. In: Presented at the SPE Asia Pacific Oil and Gas Conference and Exhibition, pp. 22–24 October. https://doi.org/10.2118/158884-MS. Perth, Australia.

Jia, B., Tsau, J.S., Barati, R., 2018. Role of molecular diffusion in heterogeneous, naturally fractured shale reservoirs during CO2 huff-n-puff. J. Petrol. Sci. Eng. 164, 31–42. https://doi.org/10.1016/j.petrol.2018.01.032.

Kerkhof, P.J., Geboers, M.A., 2005. Analysis and extension of the theory of multicomponent fluid diffusion. Chem. Eng. Sci. 60 (12), 3129–3167. https://doi.org/10.1016/j.ces.2004.12.042.

Khorsandi, S., Ahmadi, K., Johns, R.T., 2014. Analytical solutions for gas displacements with bifurcating phase behavior. SPE J. 19 (5), 943–955, 10.2118/166487-PA.

Kooijman, H.A., Taylor, R., 1991. Estimation of diffusion coefficients in multicomponent liquid systems. Ind. Eng. Chem. Res. 30 (6), 1217–1222. https://doi.org/10.1021/ie00054a023.

Krishna, R., Wesselingh, J.A., 1997. The Maxwell-Stefan approach to mass transfer. Chem. Eng. Sci. 52 (6), 861–911. https://doi.org/10.1016/S0009-2509(96)00458-7.

Kumar, A., Okuno, R., 2015. Direct perturbation of the Peng-Robinson attraction and covolume parameters for reservoir fluid characterization. Chem. Eng. Sci. 127 (4), 293–309. https://doi.org/10.1016/j.ces.2015.01.032.

Leahy-Dios, A., Firoozabadi, A., 2007. Unified model for nonideal multicomponent molecular diffusion coefficients. AIChE J. 53 (11), 2932–2939. https://doi.org/10.1002/aic.11279.

Lohrenz, J., Bray, B.G., Clark, C.R., 1964. Calculating viscosities of reservoir fluids from their compositions. J. Petrol. Technol. 16 (10), 1–171. https://doi.org/10.2118/915-PA.

Mason, E.A., Malinauskas, A.P., 1983. Gas Transport in Porous Media: the Dusty Gas Model. Elsevier, Amsterdam, The Netherlands.

Mohebbinia, S., Wong, T., 2017. Molecular diffusion calculations in simulation of gasfloods in fractured reservoirs. In: Presented at the SPE Reservoir Simulation Conference. https://doi.org/10.2118/182594-MS. Montgomery, Texas, 20-22 February.

Moortgat, J., Firoozabadi, A., 2010. Higher-order compositional modeling with Fickian diffusion in unstructured and anisotropic media. Adv. Water Resour. 33 (9), 951–968. https://doi.org/10.1016/j.advwatres.2010.04.012.

Neshat, S.S., Okuno, R., Pope, G.A., 2018. A rigorous solution to the problem of phase behavior in unconventional formations with high capillary pressure. SPE J. 23 (4), 1438–1451, 10.2118/187260-PA.

Neshat, S.S., Okuno, R., Pope, G.A., 2020. Simulation of solvent treatments for fluid blockage removal in tight formations using coupled three-phase flash and capillary pressure models. J. Petrol. Sci. Eng. 195, 107442–107454. https://doi.org/10.1016/j.petrol.2020.107442.

Orangi, A., Nagarajan, N.R., Honarpour, M.M., Rosenzweig, J.J., 2011. Unconventional shale oil and gas-condensate reservoir production, impact of rock, fluid, and hydraulic fractures. Texas. In: Presented at the SPE Hydraulic Fracturing Technology Conference, pp. 24–26. January, 10.2118/140536-MS.

Patzek, T., Saputra, W., Kirati, W., Marder, M., 2019. Generalized extreme value statistics, physical scaling and forecasts of oil production in the Barnett Shale. Energy Fuels 33 (12), 12154–12169. https://doi.org/10.1021/acs.energyfuels.9b01385.

Peters, E.J., 2012. Advanced Petrophysics: Dispersion, Interfacial Phenomena, vol. 2. Greenleaf Book Group.

Poling, B.E., Prausnitz, J.M., O'connell, J.P., 2001. Properties of Gases and Liquids. McGraw-Hill Education.

Robinson, D.B., Peng, D.Y., 1978. The Characterization of the Heptane and Heavier Fractions for GPA Peng-Robinson Programs. Gas Processors Association Research Report, Tulsa, Oklahoma.

Sakhaee-Pour, A., Bryant, S.L., 2012. Gas permeability of shale. SPE Reservoir Eval. Eng. 15 (4), 401–409, 10.2118/146944-PA.

Sandler, S.I., 2017. Chemical, Biochemical, and Engineering Thermodynamics. John Wiley & Sons.

Shojaei, H., Jessen, K., 2014. Diffusion and matrix-fracture interactions during gas injection in fractured reservoirs. In: Presented at the SPE Annual Technical Conference and Exhibition. https://doi.org/10.2118/169152-MS. Tulsa, Oklahoma, 12–16 April.

Šolcová, O., Šnajdaufová, H., Schneider, P., 2001. Multicomponent counter-current gas diffusion in porous solids: the Graham's-law diffusion cell. Chem. Eng. Sci. 56 (17), 5231–5237. https://doi.org/10.1016/S0009-2509(01)00149-X.

Taylor, R., Krishna, R., 1993. Multicomponent Mass Transfer, vol. 2. John Wiley & Sons.

Tran, S., Yassin, M.R., Eghbali, S., Doranehgard, M.H., Dehghanpour, H., 2021. Quantifying oil-recovery mechanisms during natural-gas huff 'n' puff experiments on ultratight core plugs. SPE J. 26 (1), 498–514, 10.2118/200341-PA.

Wan, T., Sheng, J., 2015. Compositional modelling of the diffusion effect on EOR process in fractured shale-oil reservoirs by Gasflooding. J. Can. Petrol. Technol. 54 (2), 107–115. https://doi.org/10.2118/2014-1891403-PA.

Wang, S., Feng, Q., Javadpour, F., Xia, T., Li, Z., 2015. Oil adsorption in shale nanopores and its effect on recoverable oil-in-place. Int. J. Coal Geol. 147, 9–24. https://doi.org/10.1016/j.coal.2015.06.002.

Yanze, Y., Clemens, T., 2012. The role of diffusion for nonequilibrium gas injection into a fractured reservoir. SPE Reservoir Eval. Eng. 15 (1), 60–71. https://doi.org/10.2118/142724-PA.

Zhang, P., Hu, L., Meegoda, J.N., Gao, S., 2015. Micro/nano-pore network analysis of gas flow in shale matrix. Sci. Rep. 5 (1), 1–11. https://doi.org/10.1038/srep13501.